Energy 116 (2016) 1131–1144

Contents lists available at ScienceDirect

Energy

journal homepage: www.elsevier.com/locate/energy

PEM fuel cell model and simulation in Matlab–Simulink based on physical parameters

Z. Abdin, C.J. Webb, E.MacA. Gray*

Queensland Micro- and Nanotechnology Centre, Griffith University, Nathan 4111, Australia

ARTICLE INFO

Article history:
Received 22 March 2016
Received in revised form
4 October 2016
Accepted 12 October 2016
Available online 24 October 2016

Keywords:
Fuel cell
Anode
Cathode
PEM
Overpotential
Modelling

ABSTRACT

An advanced PEM fuel cell mathematical model is described and realised in four ancillaries in the Matlab–Simulink environment. Where possible, the model is based on parameters with direct physical meaning, with the aim of going beyond empirically describing the characteristics of the fuel cell. The model can therefore be used to predict enhanced performance owing to, for instance, improved electrode materials, and to relate changes in the measured performance to internal changes affecting influential physical parameters. Some simplifying assumptions make the model fairly light in computational demand and therefore amenable to extension to simulate an entire fuel-cell stack as part of an energy system. Despite these assumptions, the model emulates experimental data well, especially at high current density. The influences of pressure, temperature, humidification and reactant partial pressure on cell performance are explored. The dominating effect of membrane hydration is clearly revealed.

1. Introduction

The minimal generation of by-products (ideally only water for hydrogen fuel) and the high electricity generation efficiency of the hydrogen fuel cell make this technology attractive for a range of applications such as automobiles and small-scale stationary electricity generation. Based on the lower heating value of hydrogen, fuel cells have conversion efficiencies of 40–60%, higher than most other energy conversion systems [1].

The solid polymer membrane makes the PEM fuel cell simpler and less hazardous than the alkaline type, although the PEM type is more difficult to manage because of the need for proper hydration of the membrane [2].

PEM fuel cell performance is conveniently visualized *via* the different overpotentials/voltage drops, *i.e.* the difference between the electrode potential and the equilibrium potential. An important goal of fuel cell design is to minimise the lossy contributions to the overpotential for a given current and so maximise efficiency. Membrane hydration, achieved *via* humidification of the reactant gases, plays a dominating role in PEM fuel cell performance. Too little water leads to dehydration and high membrane resistance. Excessive water leads to flooding of the electrode pores and increased electrode resistance. Hence water management, and *via* the partial vapour pressure thermal management, are critical to the good performance of PEM fuel cells.

Better design, selection of appropriate materials and optimization of the overpotential are necessary in order to improve the PEM fuel cell performance. These issues can only be addressed efficiently if realistic mathematical process models are available to predict the effects of different materials, construction and so on. A realistic model provides a framework not only for analysing the overall performance of the PEM fuel cell, but also for studying its various components and their mutual influences. An effective model thus becomes a research tool to explore parameters which are difficult to measure *e.g.* water concentration at the membrane–electrode interface, water uptake into the channel, *etc.*

In the past two decades many fuel-cell models have been presented in the literature. The early history of PEM fuel-cell modelling work has been reviewed by Bıyıkoğlu [3]. The advantages and disadvantages of various conceptual approaches to PEM fuel-cell modelling have been discussed by Cheddie and Munroe [4].

More recently, Djilali and Lu [5] and Costamagna [6] proposed a multi-dimensional model and more complex approaches in 3D modelling have also been developed for the PEM fuel cell [7–13]. Sophisticated modelling approaches have been applied to understanding various aspects of fuel-cell behaviour. Carton and Olabi

* Corresponding author.
E-mail address: e.gray@griffith.edu.au (E.MacA. Gray).

http://dx.doi.org/10.1016/j.energy.2016.10.033
0360-5442/

Glossary

A	Active area of MEA, cm^2
a	Water activity
C	Molar Concentration, mol m^{-3}
D	Diffusion coefficient, m^2 s^{-1}
E	Cell potential, V
E_c	Activation energy, kJ mol^{-1}
F	Faraday constant, 96485 C mol^{-1}
G	Gibbs free energy of activation, kJ mol^{-1}
I	Current, A
i	Current density, A cm^{-2}
i_0	Exchange current density, A cm^{-2}
k	Reaction rate coefficient
MEA	Membrane electrode assembly
$\dot{N}$	Molar flow rate, mol s^{-1}
n	Molar flux, mol m^{-2}-s
P	Pressure, atm
p	Partial pressure, atm
p_{sat}	Saturation pressure, atm
R	Universal gas constant, 8.3144 J $mol^{-1}K^{-1}$
S	Stoichiometry ratio
T	Temperature, K
X	Molar fraction
δ	Thickness, mm
ρ	Density of water, kg m^{-3}
σ_{mem}	PEM conductivity, S m^{-1}
n_d	Electro-osmotic drag coefficient
α	Charge transfer coefficient
λ	Degree of humidification
φ	Relative humidity
γ	Roughness factor
ε	Porosity
ξ	Tortuosity

[14] developed a 3D model based on computational fluid dynamics (CFD) for open pore cellular foam material as a flow plate and they found that the reactant gases were uniformly distributed from inlet to outlet. The volume-of-fluid (VOF) method has been used to numerically investigate the two-phase flow in an anode gas channel of a PEM fuel cell by Ferreira, Falcão [15]. They found that for hydrophilic or hydrophobic channel walls water moves as a film or droplets respectively. Carton, Lawlor [16] also developed a model based on CFD and VOF to investigate water droplet movement and slug formation in PEM fuel cell mini-channels. Kang [17] developed a quasi-three dimensional dynamic model to investigate the transient behaviour and dynamic characteristics of a PEM fuel cell. Xing, Cai [18] developed a 2D model to investigate the effects of relative humidity, stoichiometric flow ratio and channel length, as well as their interactive influence, on the performance of a PEM fuel cell. Salva, Iranzo [19] developed a one dimensional model to investigate the effect of relative humidity on the performance of a PEM fuel cell and validated it using neutron imaging. Abdollahzadeh, Pascoa [20] developed a multi-component mixture model to simulate two phase flow and transport in the cathode gas diffusion layer of a PEM fuel cell.

Liu, Li [21] used a numerical model to optimise flow channel dimensions for best fuel cell performance. The latter model provides a simple example of the inclusion of physical parameters so that the origin of the improved performance is identifiable as a physical entity. In contrast, in empirical modelling the improved performance of a real fuel cell owing to, for instance, a better electrocatalyst, does not directly associate the improvement with its physical origin, since it manifests in the model as parameters that may have no direct physical meaning. Ref. [11], based on empirical equations and requiring high-performance computing, exemplifies this approach.

Generally, a multi-dimensional model is useful, perhaps necessary, in order to understand the detailed behaviour of the individual elements of a fuel cell, electrolyser, *etc.* and to guide the process of designing for enhanced performance. However, to model an entire energy system in this way would be very cumbersome. Thus there is a role for realistic modelling that is not overly computation-intensive, so that a whole-of-system model becomes feasible with commonly available computing resources. A recent comparison of 1D and 3D fuel-cell models by Shekhar [22] concludes that 1D models are useful and cost-effective for practical applications, such as relating fuel-cell performance to the operating and underlying physical parameters.

This paper continues a series in which mutually compatible modular models of the components of an energy system, specifically one incorporating solar-derived hydrogen [23], are presented. One overall objective is to link the suite of component models together to form a whole-of-system model and simulation that can realistically predict the behaviour of a planned energy system, as a prerequisite to specifying the characteristics and capacities (sizes) of its components. Alternatively, such a model can simulate the behaviour of an existing energy system for research and other purposes. The component models are realised in Simulink® and are fully described so they can be recreated and used by others. The first such model [24] is of a PEM electrolyser cell. The next, for the PEM fuel cell, is presented here.

A second very important objective of the work is to use the component models as research tools to predict the effects of influential design parameters, materials and environmental conditions, thus lessening the need for experimentation, which is expensive and time-consuming.

Design parameters are necessarily physical in nature. The key to achieving the second objective is therefore to place the equations that embody the characteristics of the various elements of the electrolyser, fuel cell *etc.* on a proper physical basis by embedding the theory of the underlying physical mechanisms. Doing this has significant advantages. Firstly, it makes the model more generic in its application, in contrast to the present general reliance on empirical equations, with coefficients lacking physical significance, that only describe the characteristics of the particular component under consideration, perhaps with no applicability to the greater class of such components. Secondly, a sound physical basis for the model better allows the effects of changing materials, dimensions *etc.* to be predicted in the quest for enhanced performance, by performing sensitivity analyses, for instance, as was demonstrated in our paper on PEM electrolysers [24].

A third benefit is that a realistic model may be used to diagnose problems in the modelled component or system *via* changes in the fitted parameters arising from, for instance, degradation of an electrode, potentially allowing the degradation to be traced to its physical origin.

An example relevant to both electrolysers and fuel cells is the atomic-level mechanisms that control membrane processes

(humidification, diffusion, conductivity). In the fuel-cell case, these are represented in all existing models known to the authors (largely including this one) by purely descriptive empirical equations that do not show how the underlying mechanisms control the flow of charge. This is unsatisfactory and further work is needed to develop physically-based equations for modelling membrane processes in both fuel cells and electrolysers.

In line with the objectives outlined above, a new one-dimensional mathematical model of a PEM fuel cell is described and embedded in a simulation in the Simulink® environment. This model is distinguished from the many other PEM fuel-cell models in the literature by (i) contributions to the overpotential being tied to physically meaningful parameters wherever possible; (ii) the ability to estimate the values of physical parameters that are difficult to access directly by experiment; (iii) simplifications that reduce the computing demand without significantly impacting the ability to simulate real fuel-cell performance, making it feasible to embed the model as a module in the model of an entire energy system; (iv) utility in analysing the sensitivity of the overall performance to changes in particular physical parameters; (v) utility in relating changes in the performance of a fuel cell to the changed characteristics of an internal component owing to ageing, for instance. Despite the simplifications listed in the next section, the influences of pressure, temperature and humidification on the cell performance are captured in the new model with good fidelity. The model is validated against experimental results and then used to explore the influence of operational parameters (pressure, temperature, and humidification) on the cell polarisation curve.

2. Model development

The typical fuel cell shown in Fig. 1 is broken into four ancillaries for modelling purposes: *anode*, *cathode*, *membrane* and *voltage*. The molar balance of reactant species and their partial pressures are modelled in the anode and cathode ancillaries. The water transport mechanism and water uptake into the membrane are modelled in the membrane ancillary. The voltage ancillary models the overpotential.

The humidified hydrogen is fed to the anode and oxidized on the anode according to Eq. (1). Humidified oxygen/air is fed to the cathode and reduced on the cathode according to Eq. (2), forming water and producing heat:

$$\text{Anode}: \ H_2 \rightarrow 2H^+ + 2e^- \tag{1}$$

$$\text{Cathode}: \ \frac{1}{2}O_2 + 2e^- + 2H^+ \rightarrow H_2O \tag{2}$$

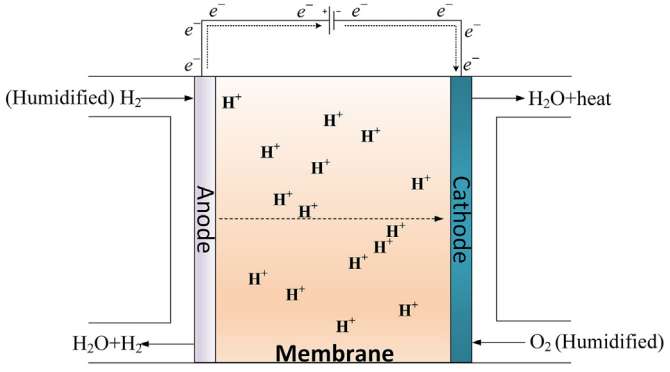

Fig. 1. Schematic of the PEM fuel cell.

Protons are transported from the anode to the cathode through the electrolyte membrane (a polymer of persulfonic acid groups with a Teflon backbone) and the electrons are carried to the cathode through the external circuit.

The mathematical model has been developed based on the following simplifying assumptions, without losing any essential contribution to the cell performance.

a) The model is one dimensional and the current is uniformly distributed (*i.e.* $I = iA$), so the gases are considered to be uniformly distributed in the cell with constant pressure.
b) The humidified reactant gases (*i.e.* hydrogen at anode and oxygen at cathode) are in equilibrium with liquid water.
c) The water activity is uniform across the membrane and is in equilibrium with the water activity at the cathode and anode catalyst layer.
d) Water is present as vapour at the membrane–electrode interface. This is equivalent to limiting the relative humidity to 100%. Thus the effect of cathode flooding when the partial pressure of water exceeds the saturation vapour pressure is not predicted quantitatively. This assumption is justifiable for fuel cells operating at moderately elevated temperatures, above about 40 °C [25] which is likely to be the case in most real installations, where the cell temperature is higher than the coolant temperature, which is higher than the ambient temperature. Water may condense in the cathode channel, but as long as it is effectively removed will not compromise the electrochemical characteristics of the membrane–cathode interface.
e) There is no pressure gradient between the anode and cathode (*i.e.* H_2 and O_2 are fed at the same pressure), so convection is not incorporated and only diffusion is considered for gas transport.
f) The anode, cathode and membrane are at the same temperature.
g) The PEM is not electrically conductive and is impermeable to neutral reactant gases and so there are no internal currents and no fuel crossover losses.

2.1. Anode ancillary

The molar balance equations for the anode are given by

$$\frac{dN_{H_2}}{dt} = \dot{N}_{H_2,in} - \dot{N}_{H_2,out} - \dot{N}_{H_2}^{cons} \tag{3}$$

$$\frac{dN_{H_2O}^{an}}{dt} = \dot{N}_{H_2O,in}^{an} - \dot{N}_{H_2O,out}^{an} - \dot{N}_{H_2O}^{mem} \tag{4}$$

where $\dot{N}_{H_2,in}$, $\dot{N}_{H_2,out}$, $\dot{N}_{H_2O,in}^{an}$, $\dot{N}_{H_2O,out}^{an}$ are anode the inlet and outlet molar flow rates of hydrogen and water respectively, $\dot{N}_{H_2}^{cons}$ is the molar flow rate of consumed hydrogen at the anode and $\dot{N}_{H_2O}^{mem}$ is the molar flow rate of membrane water from anode to cathode. The mechanism of water transport is considered later.

According to Faraday's law the molar flow rate of hydrogen at the anode inlet is

$$\dot{N}_{H_2,in} = S_{H_2} \times N_{H_2}^{cons} = S_{H_2} \times \frac{I}{2F} \tag{5}$$

Because of assumption (b), the molar fraction of water at the anode inlet is

$$X_{H_2O,in}^{an} = \frac{\varphi_{an} p_{sat}(T)}{P_{an}} \tag{6}$$

where φ_{an} is the relative humidity (*i.e.* the ratio of the partial pressure of water to the saturated vapour pressure of water) at anode, $p_{sat}(T)$ is the saturation pressure and P_{an} is the anode pressure.

The fractional ratio of the water to hydrogen gives the molar flow rate of water at the anode inlet is

$$\dot{N}^{an}_{H_2O,in} = \frac{X^{an}_{H_2O,in}}{1 - X^{an}_{H_2O,in}} \times \dot{N}_{H_2,in} = S_{H_2} \times \frac{I}{2F} \times \frac{\varphi_{an} p_{sat}(T)}{P_{an} - \varphi_{an} p_{sat}(T)} \quad (7)$$

Thus the net molar flow rate at the anode inlet can be written as

$$\dot{N}_{in,an} = S_{H_2} \times \frac{I}{2F}\left[1 + \frac{\varphi_{an} p_{sat}(T)}{P_{an} - \varphi_{an} p_{sat}(T)}\right] \quad (8)$$

where I is the current through the cell, S_{H_2} is the stoichiometry ratio (*i.e.* the ratio of the inlet flow rate of hydrogen to the rate at which it is consumed). The molar flow rates of hydrogen and water at the anode outlet are then

$$\dot{N}_{H_2,out} = (S_{H_2} - 1) \times \frac{I}{2F} \quad (9)$$

$$\dot{N}^{an}_{H_2O,out} = \dot{N}^{an}_{H_2O,in} - \dot{N}^{mem}_{H_2O} \quad (10)$$

The molar flow rate of membrane water $\dot{N}^{mem}_{H_2O}$ will be described detail in § 2.3 and the molar flow rate at the anode outlet can be written as

$$\dot{N}_{out,an} = \dot{N}_{H_2,out} + \dot{N}^{an}_{H_2O,out} \quad (11)$$

The molar flux of hydrogen through the anode can be expressed as

$$n_{H_2} = \frac{\dot{N}_{H_2,in}}{A} \quad (12)$$

and the molar flux of water through the anode can be expressed as

$$n^{an}_{H_2O} = \frac{\dot{N}^{an}_{H_2O,in}}{A} \quad (13)$$

The partial pressure of hydrogen and water at the anode is given by

$$p_i = X_i P_{an} \quad (14)$$

where p_i is the partial pressure of the hydrogen and water, X_i is the molar fraction of the hydrogen and water and P_{an} is the pressure at the anode. The molar fractions at the anode are

$$X_{H_2} = \frac{n_{H_2}}{n_{H_2} + n^{an}_{H_2O}} \quad (15)$$

$$X^{an}_{H_2O} = \frac{n^{an}_{H_2O}}{n_{H_2} + n^{an}_{H_2O}} \quad (16)$$

2.2. Cathode ancillary

The material balance equations for the cathode are given by

$$\frac{dN_{O_2}}{dt} = \dot{N}_{O_2,in} - \dot{N}_{O_2,out} - \dot{N}^{cons}_{O_2} \quad (17)$$

$$\frac{dN^{cat}_{H_2O}}{dt} = \dot{N}^{cat}_{H_2O,in} - \dot{N}^{cat}_{H_2O,out} + \dot{N}^{gn}_{H_2O} + \dot{N}^{mem}_{H_2O} \quad (18)$$

where $\dot{N}_{O_2,in}$, $\dot{N}_{O_2,out}$, $\dot{N}^{cat}_{H_2O,in}$, $\dot{N}^{cat}_{H_2O,out}$ are the cathode inlet and outlet molar flow rates of oxygen and water respectively, $\dot{N}^{cons}_{O_2}$ is the molar flow rate of consumed oxygen at the cathode, $\dot{N}^{gn}_{H_2O}$ is the molar flow rate of generated water at the cathode and $\dot{N}^{mem}_{H_2O}$ is the membrane molar flow rate of water from anode to cathode through the membrane.

The molar flow rates of oxygen and water at the cathode inlet are

$$\dot{N}_{O_2,in} = S_{O_2} \times \dot{N}^{cons}_{O_2} = S_{O_2} \times \frac{I}{4F} \quad (19)$$

$$\dot{N}^{cat}_{H_2O,in} = S_{O_2} \times \frac{I}{4F} \times \frac{\varphi_{cat} P_{sat}(T)}{P_{cat} - \varphi_{cat} P_{sat}(T)} \quad (20)$$

and so the net molar flow rate at the cathode inlet can be written as

$$\dot{N}_{in,cat} = S_{O_2} \times \frac{I}{4F}\left[1 + \frac{\varphi_{cat} P_{sat}(T)}{P_{cat} - \varphi_{cat} P_{sat}(T)}\right] \quad (21)$$

At the cathode side the molar flow rate of water is the sum of water generated by the reaction, the water transported from anode to cathode and the water at the cathode inlet *i.e.*

$$\dot{N}_{H_2O,cat} = \dot{N}^{gn}_{H_2O} + \dot{N}^{mem}_{H_2O} + \dot{N}^{cat}_{H_2O,in} \quad (22)$$

The molar flow rate of generated water is

$$\dot{N}^{gn}_{H_2O} = \frac{I}{2F} \quad (23)$$

and the resultant molar flux of water through the cathode is

$$n_{H_2O,cat} = \frac{\dot{N}_{H_2O,cat}}{A} = \frac{\dot{N}^{gn}_{H_2O} + \dot{N}^{mem}_{H_2O} + \dot{N}^{cat}_{H_2O,in}}{A} \quad (24)$$

and the molar flux of oxygen through the cathode is

$$n_{O_2} = \frac{\dot{N}_{O_2,in}}{A} \quad (25)$$

The partial pressure of species at the cathode can be calculated according to Eq. (14). The molar fractions at the cathode can be expressed as

$$X_{O_2} = \frac{n_{O_2}}{n_{O_2} + n^{cat}_{H_2O}} \quad (26)$$

$$X^{cat}_{H_2O} = \frac{n^{cat}_{H_2O}}{n_{O_2} + n^{cat}_{H_2O}} \quad (27)$$

2.3. Membrane ancillary

The solid electrolyte in a PEM fuel cell is typically a perfluorinated ionomer, Nafion®, for example. An inert but chemically stable polymer backbone which is not ionically conductive provides chemical stability and durability. Side chains of sulfonic acid bonded to the backbone enable ionic conduction. The SO_3^- chains are distributed as generally isolated clusters in the membrane [30].

2.3.1. Proton transport

When the Nafion® structure is hydrated, the hydrophilic sulfonic acid chains absorb water and promote proton transport by two mechanisms. At low hydration levels, vehicular transport occurs by diffusion. At high hydration levels, the Grotthuss (proton hopping) mechanism is more effective because of the enhanced connectivity between SO_3^- clusters in the highly hydrated environment [26–28]. Membrane hydration is therefore a crucially important parameter.

Membrane water content was measured by Springer, Zawodzinski [29] as a function of water activity (a) *i.e.* relative humidity (φ) for the Nafion® 117 membrane. Water content/degree of humidification (λ) of the membrane is defined as the number of water molecules per sulfonic acid site, $\lambda = \frac{H_2O}{SO_3^-H^+}$. The water uptake of a Nafion® membrane at 30 °C in contact with a gas-phase flow was described empirically [29] by

$$\lambda = 0.043 + 17.18\varphi - 39.85\varphi^2 + 36.0\varphi^3 \text{ for } 0 \le \varphi \le 1 \qquad (28)$$

Though Eq. (28) was derived for 30 °C, it has been applied to higher temperature conditions as well. In the fully humidified condition (100% relative humidity, vapour-equilibrated water content), Eq. (28) implies a maximum achievable water humidification $\lambda \approx 14$. In practice, however λ decreases with increasing temperature, to around 10 at 80 °C. The uptake of Nafion® equilibrated with liquid water is much higher, $\lambda \approx 22$. This difference between the water- and vapour-equilibrated conditions is a result of Schroeder's paradox [30–32].

2.3.2. Water transport

Water transport across the membrane occurs *via* four distinct processes: electro-osmotic drag, diffusion, hydraulic pressure and thermo-osmosis, as illustrated in Fig. 2. Firstly, the electro-osmotic drag is a potential-driven flow of water resulting from the attraction of polar water molecules to the protons passing from the anode to the cathode. Secondly, diffusion occurs as a result of the gradient of water concentration across the membrane. Because the water concentration is usually higher at the cathode owing to water generation in the cathode catalyst layer, this transport occurs from the cathode to the anode and is therefore referred to as back-diffusion. Thirdly, any pressure difference between the anode and cathode drives water across the membrane towards the low-pressure side. Finally, thermo-osmosis is a temperature gradient flow through the membrane, *i.e.* the flow of water across the membrane against the hydrostatic pressure [28]. Combining the four water transport mechanisms and defining flow from the anode to the cathode as positive, the net molar flow rate of water through the membrane, $\dot{N}_{H_2O}^{mem}$ is

$$\dot{N}_{H_2O}^{mem} = \dot{N}_{H_2O}^{eod} - \dot{N}_{H_2O}^{bd} \pm \dot{N}_{H_2O}^{hp} \pm \dot{N}_{H_2O}^{temp} \qquad (29)$$

where $\dot{N}_{H_2O}^{eod}$ is the molar flow rate due to electro-osmotic drag, $\dot{N}_{H_2O}^{bd}$ is due to back-diffusion, $\dot{N}_{H_2O}^{hp}$ is due to the pressure difference and $\dot{N}_{H_2O}^{temp}$ is the molar flow rate of water due to thermo-osmosis. In practice, electro-osmotic drag and back-diffusion are the dominant mechanisms [33]. In the absence of a pressure difference between the anode and cathode then there is no pressure-driven water transport across the membrane. Most analyses have ignored thermo-osmosis because its contribution is normally small compared to those of net diffusive and electro-osmotic drag transfer. We now consider the dominant mechanisms in more detail.

2.3.2.1. Electro-osmotic drag

The electro-osmotic drag coefficient (n_d) is defined as the number of water molecules transported (dragged) per proton. Transport of water *via* this mechanism necessarily occurs from the anode to the cathode. The corresponding molar flow rate of water can be expressed as

$$\dot{N}_{H_2O}^{eod} = n_d \times \frac{i}{F} \qquad (30)$$

where i is the current density. In practice, n_d is a function of the humidification (λ) of the membrane. This humidification has been reported over the years with considerable variation depending on the method of measurement and data fitting. LaConti, Fragala [34] measured the electro-osmotic drag by passing the current through the membrane and observed the level of a water column for water equilibrated conditions. They reported that the humidification/water uptake range is $15 \le \lambda \le 25$, where two to three water molecules were dragged per proton, and also concluded that the drag coefficient decreases linearly with water content of the membrane. Springer, Zawodzinski [29] and Zawodzinski Jr, Neeman [35] used the same method and measured the drag coefficient $n_d = 2.5$ for a water-equilibrated membrane (fully hydrated) and $n_d = 0.9$ for a partially hydrated membrane (*i.e.* λ=11). The empirical expression given by Springer, Zawodzinski [29] (Eq. (31) here) is used to calculate the n_d as a function of membrane humidification.

$$n_d = 2.5 \times \frac{\lambda}{22} \qquad (31)$$

2.3.2.2. Back-diffusion

The combined effects of electro-osmotic drag and water generation at the cathode tend to flood the cathode and dry-out the anode. Back-diffusion causes a counter-flow and so can partially compensate the removal of water from the anode and so flatten the water concentration profile through the membrane, especially for thinner membranes [28]. The molar flow rate of water due to back-diffusion may be calculated by integrating Fick's law through the membrane, giving

$$\dot{N}_{H_2O}^{bd} = \frac{AD_w}{\delta_{mem}} \left[C_{H_2O,mem}^{cat} - C_{H_2O,mem}^{an} \right] \qquad (32)$$

where D_w is the diffusion coefficient of water in the membrane, δ_{mem} is the membrane thickness and $C_{H_2O,mem}^{an}$, $C_{H_2O,mem}^{cat}$ are the water concentrations at the anode and cathode sides of the

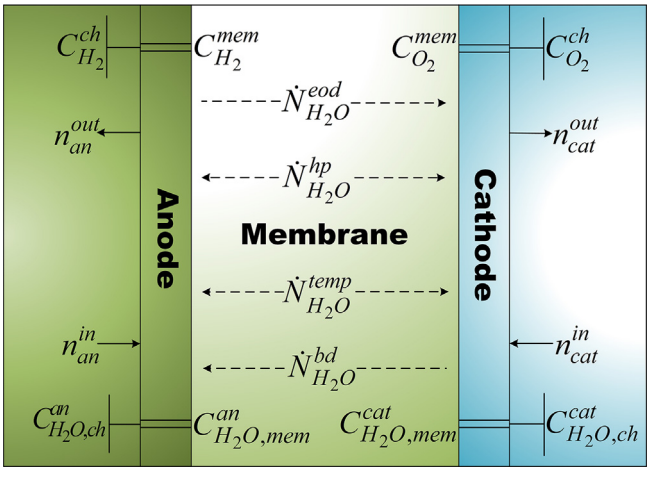

Fig. 2. Species balance within PEM fuel cell.

membrane. These concentrations can be expressed in terms of the water concentration in the electrode channels as follows

$$C^{an}_{H_2O,mem} = C^{an}_{H_2O,ch} - \frac{\delta^{an}_{el} n^{an}_{H_2O}}{D^{an}_{eff}} \tag{33}$$

$$C^{cat}_{H_2O,mem} = C^{cat}_{H_2O,ch} + \frac{\delta^{cat}_{el} n^{cat}_{H_2O}}{D^{cat}_{eff}} \tag{34}$$

where D^{an}_{eff} is the effective binary (H_2–H_2O) diffusion coefficient at the anode, D^{cat}_{eff} is the effective binary (O_2–H_2O) diffusion coefficient at the cathode, δ^{an}_{el}, δ^{cat}_{el} are the thicknesses of the anode and cathode respectively and $C^{an}_{H_2O,ch}$, $C^{cat}_{H_2O,ch}$ represent the water concentrations in the anode and cathode channels respectively.

Diffusion of a molecular species with mean free path $\bar{\lambda}$ through a porous medium with average pore radius $\bar{r}$ occurs by two principal mechanisms: molecular diffusion for $\bar{r} >> \bar{\lambda}$ and Knudsen diffusion for $\bar{r} << \bar{\lambda}$, when interactions with the pore wall occur much more frequently than collisions with other molecules. In most porous structures, both mechanisms are significant [36]. The effective binary diffusion coefficient of water at the anode and cathode can be expressed as [36]

$$\frac{1}{D^{an}_{eff}} = \frac{\varepsilon}{\xi}\left(\frac{1}{D^{H_2-H_2O}_{eff}} + \frac{1}{D^{H_2O,K}_{eff}}\right) \tag{35}$$

$$\frac{1}{D^{cat}_{eff}} = \frac{\varepsilon}{\xi}\left(\frac{1}{D^{O_2-H_2O}_{eff}} + \frac{1}{D^{H_2O,K}_{eff}}\right) \tag{36}$$

where ε/ξ is the ratio of electrode porosity to tortuosity, $D^{H_2-H_2O}_{eff}$ is the effective molecular diffusion coefficient for the H_2–H_2O binary system, $D^{O_2-H_2O}_{eff}$ is the effective molecular diffusion coefficient for the O_2–H_2O binary system and $D^{H_2O,K}_{eff}$ is the effective Knudsen diffusion coefficient for water.

For Knudsen diffusion, the transport of molecules can be modelled using kinetic theory [37,38], since the gas molecules frequently collide with the walls of the pores, giving

$$D^{H_2O,K}_{eff} = \frac{4}{3}\bar{r}\sqrt{\frac{8RT}{\pi M_{H_2O}}} \tag{37}$$

where $\bar{r}$ is the mean pore radius and M_{H_2O} is the molar weight of H_2O. Using the Chapman-Enskog theory of the ideal gas, the effective molecular binary diffusion coefficients, $D^{H_2-H_2O}_{eff}$ and $D^{O_2-H_2O}_{eff}$ can be expressed as [37,39]

$$D^{H_2-H_2O}_{eff} = 0.00133\left(\frac{1}{M_{H_2}} + \frac{1}{M_{H_2O}}\right)^{1/2}\frac{T^{3/2}}{P_{an}\,\sigma^2_{H_2-H_2O}\,\Omega_D} \tag{38}$$

$$D^{O_2-H_2O}_{eff} = 0.00133\left(\frac{1}{M_{O_2}} + \frac{1}{M_{H_2O}}\right)^{1/2}\frac{T^{3/2}}{P_{cat}\,\sigma^2_{O_2-H_2O}\,\Omega_D} \tag{39}$$

where M_{H_2} and M_{O_2} are the molar weights of H_2 and O_2, $\sigma_{H_2-H_2O}$ and $\sigma_{O_2-H_2O}$ are the mean molecular radii of species H_2–H_2O and O_2–H_2 and Ω_D is a dimensionless diffusion collision integral. Ω_D, $\sigma_{H_2-H_2O}$ and $\sigma_{O_2-H_2O}$ can be expressed analytically as [40]

$$\Omega_D = \frac{1.06}{\tau^{0.156}} + \frac{0.193}{\exp(0.476\tau)} + \frac{1.036}{\exp(1.53\tau)} + \frac{1.765}{3.894\tau} \tag{40}$$

$$\begin{aligned}\sigma_{H_2-H_2O} &= \frac{\sigma_{H_2} + \sigma_{H_2O}}{2}\\ \sigma_{O_2-H_2O} &= \frac{\sigma_{O_2} + \sigma_{H_2O}}{2}\end{aligned} \tag{41}$$

$$\begin{aligned}\tau_{H_2-H_2O} &= \frac{kT}{\varepsilon_{H_2-H_2O}}\\ \tau_{O_2-H_2O} &= \frac{kT}{\varepsilon_{O_2-H_2O}}\end{aligned} \tag{42}$$

and the Lennard-Jones energies $\varepsilon_{H_2-H_2O}$ and $\varepsilon_{O_2-H_2O}$ can be expressed as

$$\begin{aligned}\varepsilon_{H_2-H_2O} &= \sqrt{\varepsilon_{H_2}\varepsilon_{H_2O}}\\ \varepsilon_{O_2-H_2O} &= \sqrt{\varepsilon_{O_2}\varepsilon_{H_2O}}\end{aligned} \tag{43}$$

The values of σ_{H_2}, σ_{O_2} and σ_{H_2O} are 2.827 Å, 3.467 Å and 2.641 Å, respectively [41]. The Lennard-Jones potentials, ε_i/k, for H_2, O_2 and H_2O are 59.7, 106.7 and 809.1 K, respectively. The values of $D^{H_2-H_2O}_{eff}$ and $D^{O_2-H_2O}_{eff}$ can be obtained by solving Eqs. (35) and (43).

The water concentration at the anode and cathode channels can be expressed as

$$C^{an}_{H_2O,ch} = \frac{\rho_{H_2O}(T_{an})}{M_{H_2O}} \tag{44}$$

$$C^{cat}_{H_2O,ch} = \frac{\rho_{H_2O}(T_{cat})}{M_{H_2O}} \tag{45}$$

where ρ_{H_2O} is the water density and T_{an} and T_{cat} are the temperatures of the anode and cathode respectively.

Substituting Eqs. (44) and (45) into Eqs. (33) and (34)

$$C^{an}_{H_2O,mem} = \frac{\rho_{H_2O}(T_{an})}{M_{H_2O}} - \frac{\delta^{an}_{el} n^{an}_{H_2O}}{D^{an}_{eff}} \tag{46}$$

$$C^{cat}_{H_2O,mem} = \frac{\rho_{H_2O}(T_{cat})}{M_{H_2O}} + \frac{\delta^{cat}_{el} n^{cat}_{H_2O}}{D^{cat}_{eff}} \tag{47}$$

Now Eq. (32) can be written as

$$\dot{N}^{bd}_{H_2O} = \frac{AD_w}{\delta_{mem}}\left(\left[\frac{\rho_{H_2O}(T_{cat})}{M_{H_2O}} + \frac{\delta^{cat}_{el} n^{cat}_{H_2O}}{D^{cat}_{eff}}\right] - \left[\frac{\rho_{H_2O}(T_{an})}{M_{H_2O}} - \frac{\delta^{an}_{el} n^{an}_{H_2O}}{D^{an}_{eff}}\right]\right) \tag{48}$$

The net molar rate through the membrane [Eq. (29)] becomes

$$\dot{N}^{mem}_{H_2O} = n_d \times \frac{i}{F} - \frac{AD_w}{\delta_{mem}}\left(\left[\frac{\rho_{H_2O}(T_{cat})}{M_{H_2O}} + \frac{\delta^{cat}_{el} n^{cat}_{H_2O}}{D^{cat}_{eff}}\right] - \left[\frac{\rho_{H_2O}(T_{an})}{M_{H_2O}} - \frac{\delta^{an}_{el} n^{an}_{H_2O}}{D^{an}_{eff}}\right]\right) \tag{49}$$

2.4. Voltage ancillary

The output voltage of a fuel cell can be expressed as

$$E = E_{oc} - E_{ovp} \tag{50}$$

where E_{oc} is the open-circuit voltage of the cell and E_{ovp} is the voltage loss or overpotential due to electro catalyst layers, electron migration in the bipolar plates and electrode backing and proton migration in the PEM.

The open-circuit voltage of PEM fuel cell in the temperature range of 23–120 °C was found to be temperature dependent, with values always lower than the theoretically expected values. To date, a quantitative explanation for open-circuit voltage behaviour has not been provided. One explanation attributes this behaviour to H_2 crossover and/or internal current, as described by Larminie, Dicks [42]. However, in reality, there are several voltage losses within a fuel cell that cause the actual cell voltage to be less than the open-circuit cell voltage. The cell voltage losses or overpotentials are composed of activation overpotential (E_{act}) due to electro catalyst layers, concentration overpotential (E_{con}) due to the mass transfer limitations at higher current densities and ohmic overpotential (E_{ohm}) due to electron migration in the bipolar plates and electrode backing and proton migration in the PEM. Now Eq. (50) can be written as

$$E = E_{oc} - E_{act} - E_{con} - E_{ohm} \tag{51}$$

2.4.1. Open-circuit voltage

The ideal cell potential/voltage is attained when the cell is in thermodynamic equilibrium. The E_{oc} is calculated from a modified form of the Nernst equation:

$$E_{oc} = E_{rev} + \frac{RT}{2F}\ln\left[p_{H_2}\sqrt{p_{O_2}}\right] \tag{52}$$

Here E_{rev} is the reversible voltage and it is the voltage that would be obtained if the Gibbs free energy could be converted directly into electrical work without any losses. An extra term is added to account for changes in reversible voltage at temperatures that deviate from the standard reference temperature and now the reversible cell potential/voltage can be expressed empirically as [43]

$$E_{rev} = E^{o}_{rev} + \left(T - T_{ref}\right) \times \frac{\Delta S^{o}}{nF} \tag{53}$$

Here E^{o}_{rev}(1.229 V) is the standard state or minimum theoretical voltage and $\frac{\Delta S^{o}}{nF}(-0.9 \times 10^{-3})$ is the standard state entropy change.

2.4.2. Activation overpotential

The rate of an electrochemical reaction is limited by the activation energy barrier to charge transfer between the electrolyte and electrode or *vice-versa*. The barrier is represented by a single transition state through which each charge must pass. The probability of having been excited to the transition state is taken to be proportional to the attempt rate and to depend exponentially on the effective barrier height and the temperature. The reactant consumption is proportional to the surface concentration [42]. The speed at which an electrochemical reaction proceeds on the electrode surface is the rate at which the electrons are released or consumed, *i.e.* the electrical current. According to transition-state theory [44] the resultant current can be written as

$$i = nF\left[k_f C_{Ox}\exp\left(\frac{-\alpha_{cat}F(E-E_0)}{RT}\right) - k_b C_{Re}\exp\left(\frac{\alpha_{an}F(E-E_0)}{RT}\right)\right] \tag{54}$$

where nF is the charge transferred, k_f is the forward reaction rate coefficient, k_b is the backward reaction rate coefficient, C_{Ox} is the surface concentration of oxidation reacting species, C_{Re} is the surface concentration of reduction reacting species and α is the charge transfer coefficient of electrode.

At equilibrium, the resultant current density is zero and the reaction proceeds in both directions at the same rate, corresponding to the exchange current density. If the exchange current density is high, the surface of the electrode is more active. The higher the exchange current density, the more active the surface of the electrode and the lower the energy barrier to charge transfer and the greater the current generated at a given overpotential [45]. At equilibrium

$$\begin{aligned} i_0 = i_0^{an} = i_0^{cat} &= nFk_o^f C_{Ox}\exp\left[\frac{-\alpha_{cat}F(E-E_0)}{RT}\right] \\ &= nFk_o^b C_{Re}\exp\left[\frac{\alpha_{an}F(E-E_0)}{RT}\right] \end{aligned} \tag{55}$$

Now Eq. (54) can be written as

$$i = i_0\left\{\exp\left[\frac{-\alpha_{cat}F(E-E_0)}{RT}\right] - \exp\left[\frac{\alpha_{an}F(E-E_0)}{RT}\right]\right\} \tag{56}$$

i.e. the Butler–Volmer equation. The deviation of electrode potential from the equilibrium potential value is the overpotential *i.e.* $E-E_0=E_{act}$. The activation overpotential (E_{act}) is associated with electrode kinetics and it plays a role at both the anode and cathode. The activation overpotential is always defined with respect to a specific reaction for which the equilibrium potential is known.

When the activation overpotential is large and negative at the cathode (*i.e.* $E<E_0$), the first term in Eq. (56) becomes predominant *i.e.* the reduction current is predominant and now Eq. (56) can be written as

$$i = i_0^{cat}\exp\left[\frac{-\alpha_{cat}F(E-E_0)}{RT}\right] = i_0^{cat}\exp\left[\frac{\alpha_{cat}FE_{act}^{an}}{RT}\right] \tag{57}$$

Similarly, when the activation overpotential is positive at the anode (*i.e.* $E>E_0$) the second term in Eq. (56) becomes predominant *i.e.* oxidation current is predominant and now Eq. (56) can be written as

$$i = -i_0^{an}\exp\left[\frac{\alpha_{an}F(E-E_0)}{RT}\right] = -i_0^{an}\exp\left[\frac{\alpha_{an}FE_{act}^{an}}{RT}\right] \tag{58}$$

Eqs. (57) and (58) give the activation overpotential for both anode and cathode:

$$E_{act}^{an} = \frac{RT}{\alpha_{an}F}\ln\left(\frac{i}{i_0^{an}}\right) \tag{59}$$

$$E_{act}^{cat} = \frac{RT}{\alpha_{cat}F}\ln\left(\frac{i}{i_0^{cat}}\right) \tag{60}$$

2.4.3. Concentration overpotential

Mass transport in the electrodes and at the membrane–electrode interfaces influences the concentrations of hydrogen and oxygen *via* an inverse relationship between the concentration of reactants on the electrode surface and the current density. In general, when the depletion rate reaches the diffusion rate, the reactant concentration falls to zero, reducing the partial pressures of the reactant gases. Thus the pressures of hydrogen and oxygen depend on the current density and on the physical properties of the electrodes and membrane. A

concentration overpotential develops when the surface coverage of oxygen bubbles at high current density prevent the hydrogen from being supplied at a higher rate, thus hindering the reaction [46]. The limiting current density is typically in the range 500–1500 mA/cm^2[47].

Mass flow through the electrodes involves two-component mixtures (H_2–H_2O at the anode; O_2–H_2O at the cathode) and is typically modelled using Fick's law, leading to effective binary diffusion coefficients for the reactants, as outlined in § 2.3.2.2. By combining Fick's law with the Nernst equation, the limiting diffusion rate at high current density can be calculated, which then allows a calculation of the potential drop caused by excess reaction products blocking access by the reactants to catalyst sites [48]. The disparate diffusion rates of hydrogen and oxygen can then be understood by applying this diffusion-driven approach to the cathode and the anode:

$$E_{con} = E_1 - E_o = \left(E_o + \frac{RT}{zF}\ln C_1\right) - \left(E_o + \frac{RT}{zF}\ln C_0\right) = \frac{RT}{zF}\ln\frac{C_1}{C_0} \tag{61}$$

where z is the number of electrons transferred during the reaction and the "0" subscript denotes a reference condition. The above equation can be applied to the anode and the cathode, giving

$$E_{con} = E_{con}^{an} + E_{con}^{cat} \tag{62}$$

$$E_{con}^{an} = \frac{RT}{2F}\ln\frac{C_{H_2}^{mem}}{C_{H_2,0}^{mem}} \tag{63}$$

$$E_{con}^{cat} = \frac{RT}{4F}\ln\frac{C_{O_2}^{mem}}{C_{O_2,0}^{mem}} \tag{64}$$

where $C_{H_2}^{mem}$ and $C_{O_2}^{mem}$ are the hydrogen and oxygen concentration at the membrane-electrode interface, respectively.

At the membrane-electrode interface the molar concentrations can be expressed as

$$C_{H_2}^{mem} = C_{H_2}^{ch} + \frac{\delta_{el}^{an} n_{H_2}}{D_{eff}^{an}} \tag{65}$$

$$C_{O_2}^{mem} = C_{O_2}^{ch} + \frac{\delta_{el}^{cat} n_{O_2}}{D_{eff}^{cat}} \tag{66}$$

The molar concentrations of oxygen and hydrogen in the channels can be expressed as

$$C_{H_2}^{ch} = \frac{P_{an} X_{H_2}}{RT} \tag{67}$$

$$C_{O_2}^{ch} = \frac{P_{cat} X_{O_2}}{RT} \tag{68}$$

Substituting Eqs (67) and (68) into Eqs (65) and (66) gives

$$C_{H_2}^{mem} = \frac{P_{an} X_{H_2}}{RT} + \frac{\delta_{el}^{an} n_{H_2}}{D_{eff}^{an}} \tag{69}$$

$$C_{O_2}^{mem} = \frac{P_{cat} X_{O_2}}{RT} + \frac{\delta_{el}^{cat} n_{O_2}}{D_{eff}^{cat}} \tag{70}$$

2.4.4. Ohmic overpotential

The electrolyte, electrocatalyst layer, gas diffusion layer (GDL), flow fields, current collectors, interfacial contacts between the components and the terminal connections all contribute to the ohmic overpotential in a PEM fuel cell. The ohmic overpotential can be divided into ionic and electrical resistance. The electrical component is the resistance of the electrically conductive cell components to the flow of electrons. The ionic resistance is due to the proton flow through the membrane. Most of the electrical resistance usually occurs due to the lack of proper contact between the GDL, bipolar plates, cooling plates and other interconnects. However, the ionic resistance dominates because the mobility of the charge carrier in an ionic conductor is much less than in an electronic conductor. An ohmic overpotential E_{ohm} arises owing to the ohmic resistance of the current collectors, bipolar plates and electrode surfaces [49]. The ohmic overpotential is (by definition assumed) linearly proportional to the current:

$$E_{ohm} = R_{cell} I \tag{71}$$

where R_{cell} is the effective ohmic resistance of the cell:

$$\begin{aligned} E_{ohm} &= \left(R_{el} + R_{pl} + R_{mem}\right) I \\ &= E_{ohm}^{el} + E_{ohm}^{pl} + E_{ohm}^{mem} \end{aligned} \tag{72}$$

Here R_{el}, R_{pl}, R_{mem} are the resistances of the electrodes, bipolar plates and membrane respectively, and E_{ohm}^{el}, E_{ohm}^{pl}, E_{ohm}^{mem} are the corresponding contributions to the ohmic overpotential.

The resistance to currents through the electrode and the flow field plate have been modelled by Marr and Li [50] in terms of an effective electrode resistivity ρ_{eff} (Fig. 3):

$$R_{el,pl} = \rho_{eff}\frac{l}{A} \tag{73}$$

where l and A are respectively the length and cross-section of the conductor and ρ_{eff} can be expressed for this two-component conductor as [50]

$$\rho_{eff} = \frac{\rho_{el}}{(1-\varepsilon)^{1.5}} \tag{74}$$

where ε is the (assumed small) electrode porosity. Marr and Li take the total average conducting path length to be $(w_c+w_s)/4$, where w_c is the channel width and w_s is the width of the channel support. The average resistance per half flow channel becomes [50]

$$R_1^{an} = \frac{\rho_{eff}\left(w_c^{an} + w_s^{an}\right)}{4\,L\,n_{ch}^{an}\,\delta_{el}^{an}} \tag{75}$$

$$R_1^{cat} = \frac{\rho_{eff}\left(w_c^{cat} + w_s^{cat}\right)}{4\,L\,n_{ch}^{cat}\,\delta_{el}^{cat}} \tag{76}$$

where L is the length of the MEA perpendicular to the plane of Fig. 3. The total flow-channel resistance for the two halves in parallel is then

$$R_{el} = \frac{\rho_{eff}}{8L}\left[\frac{\left(w_c^{an} + w_s^{an}\right)}{n_{ch}^{an}\,\delta_{el}^{an}} + \frac{\left(w_c^{cat} + w_s^{cat}\right)}{n_{ch}^{cat}\,\delta_{el}^{cat}}\right] \tag{77}$$

In Fig. 3, the resistance of the right-hand section of the flow field plate, R_2, is given for the anode and cathode by

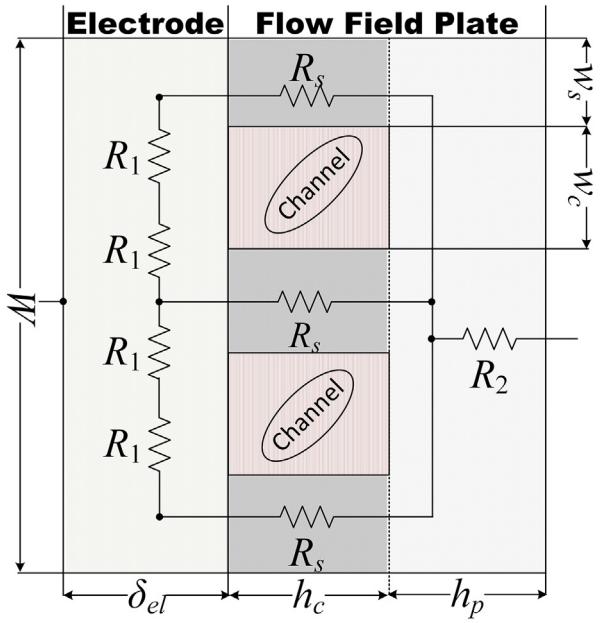

Fig. 3. Electric circuit model of the ohmic resistance of the electrode and flow field plate (after Ref. [50]).

$$R_2^{an} = \frac{\rho_p^{an}\, h_p^{an}}{W\, L} \tag{78}$$

$$R_2^{cat} = \frac{\rho_p^{cat}\, h_p^{cat}}{W\, L} \tag{79}$$

where ρ_p^{an}, ρ_p^{cat} are the respective resistivities, h_p^{an}, h_p^{cat} are the distances from the outside edge of the plate to the channel surface and W is the width of the MEA. Similarly, the resistances of the channel supports are

$$R_s^{cat} = \frac{\rho_p^{cat}\, h_c^{cat}}{n_{chs}^{cat}\, w_s^{cat}\, L} \tag{80}$$

$$R_s^{an} = \frac{\rho_p^{an}\, h_c^{an}}{n_{chs}^{an}\, w_s^{an}\, L} \tag{81}$$

where h_c^{cat}, h_c^{an} are the channel heights and n_{chs}^{an}, n_{chs}^{cat} the numbers of channel supports. The total resistance of the flow-field plate is then

$$R_{pl} = \left(R_s^{an} + R_s^{cat}\right) + \left(R_2^{an} + R_2^{cat}\right) \tag{82}$$

Marr and Li [50] showed the polarisation curve to visualize the contribution of different overpotentials. Ionic loss in the membrane is the second largest source of loss and this loss becomes more significant at high current densities. The contribution of electronic resistance to the ohmic overpotential is very small. Bernardi and Verbrugge [51] also showed that the ionic resistance constitutes the major contribution to the ohmic overpotential. Springer et al. [29,52] simply ignored the contribution of electronic resistance to the ohmic overpotential. Laurencelle, Chahine [53] and Amphlett, Baumert [54] demonstrated that the ohmic overpotential depends strongly on membrane humidity and cell temperature and several studies also showed that the ohmic overpotential is a function of the membrane conductivity *i.e.*$\sigma_{mem}(\lambda,T)$ [29,55]. Thus the dominant contribution to ohmic overpotential (E_{ohm}) is the ionic loss caused by resistance to the ion flow through the membrane. This membrane resistance can be expressed using Ohm's law in the form $\underline{i} = \sigma\ \nabla E$, as

$$\begin{aligned} E_{ohm} &= \frac{\delta_{mem} I}{A\sigma_{mem}} \\ &= \frac{\delta_{mem} i}{\sigma_{mem}} \end{aligned} \tag{83}$$

where δ_{mem} is the thickness and σ_{mem} is the conductivity of the PEM. The membrane conductivity σ_{mem} can be empirically expressed as a function of humidification/water content in the membrane [29,44] as

$$\sigma_{mem} = (0.005139\lambda - 0.00326)\exp\left[\frac{-\Delta G}{R}\left(\frac{1}{T_{ref}} - \frac{1}{T}\right)\right] \tag{84}$$

where $-\Delta G/R$=1268 K and T_{ref}=303 K.

3. Results and discussion

Fig. 4 depicts the generalized PEM fuel cell Simulink model, shows how each of the four ancillaries discussed in the previous section contributes to the simulation and maps the interactions between them.

3.1. Model parameters

To validate the model, parameters for which reliable estimates were available in the literature were fixed. These are listed in Table 1.

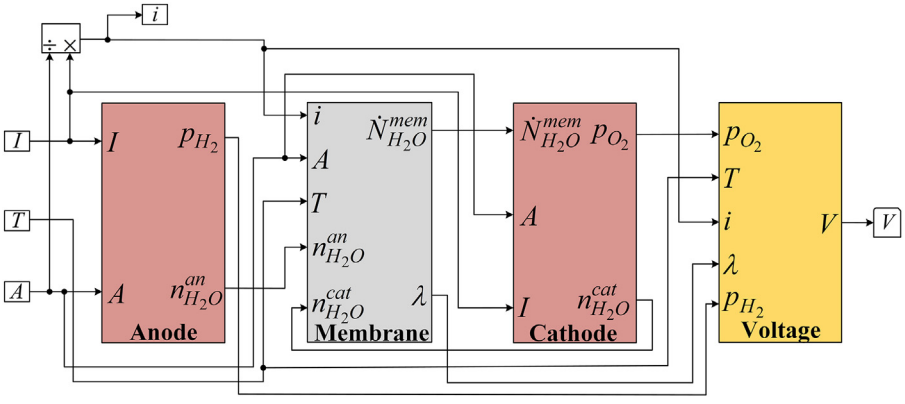

Fig. 4. Simulink model of the PEM fuel cell.

Table 1
Fixed model parameters.

Parameter	Value
A	51.84 cm^2
δ_{mem}	0.0254 cm
δ_{el}	0.008 cm
ΔG_c^{an}	29 kJ mol^{-1}
ΔG_c^{cat}	66 kJ mol^{-1}
S_{H_2}	1.2
S_{O_2}	2
ρ_{H_2O}	1 g cm^{-3}
ρ_{el}	10.6×10^{-6} Ω cm
ρ_p^{an}	16.0×10^{-3} Ω cm
ρ_p^{cat}	43.1×10^{-6} Ω cm
D_w	1.28×10^{-6} cm^2 s^{-1}
ε	0.3
ξ	4

Parameters that could not be reliably estimated, mostly because they are difficult to measure directly, were obtained by fitting the model to experimental data from Ref. [56] under standard conditions (T=25 °C, humidification at 25 °C, P=1 atm). These include the roughness factor (γ_M), charge transfer coefficients (α) and the exchange current density in the reference state (i_0^{ref}). These parameters were subsequently fixed for the comparison of the model with experimental data under other conditions, and for exploring the influences of the humidification temperature and the humidification ratio. The fitted parameter values are listed in Table 2 and compared to published values below.

The effective exchange current density depends on temperature and the electrode surface roughness factor, which is defined as the effective (electrochemical) electrode area divided by the geometrical area. If the exchange current density per actual catalyst surface area at reference temperature and pressure is i_0^{ref} , then the effective exchange current density at any temperature may be calculated, assuming an activation mechanism, as [44,57]:

$$i_0 = \gamma_M \exp\left[-\frac{\Delta G_C}{R}\left(\frac{1}{T}-\frac{1}{T_{ref}}\right)\right] i_0^{ref} \quad (85)$$

where γ_M is the electrode surface roughness factor and ΔG_C is the activation free energy. The roughness factor depends on the structure of the electrode surface. We tested our model using data from Wang, Husar [56], who used Pt loadings of 0.4 mg/cm^2 for their electrodes but did not describe their microstructure. The roughness factor can be determined experimentally [58–60] or estimated from catalyst loading, catalyst particle density and size [57]. Roughness factors for the oxygen reduction reaction are reported as 2.7 [60], 9.2 [61], 200 [58] for Pt microdisk, Pt wire and Pt powder electrodes respectively. Our fitted value $\gamma_M = 47$ (at 25 °C and 1 atm) lies in this range. The charge transfer coefficient values for anode and cathode are reported to be in the range 0–1 and 0–2 respectively [38,62–66]. Our fitted values lie within these ranges. For Pt-based electrodes, the exchange current densities for the oxygen reduction and hydrogen oxidation reactions are reported as 10^{-9}–10^{-12} and 10^{-4}–10^{-3} A cm^{-2} (at 25 °C and 1 atm) [67], respectively. Our fitted values lie within these ranges. In our view, the values of parameters obtained from a well-validated physically based model may be more reliable than those estimated from indirect experiments with many assumptions and uncertainties.

Table 2
Fitted model parameters.

Parameter	Value
$i_{0,an}^{ref}$	1×10^{-4} A cm^{-2}
$i_{0,cat}^{ref}$	1×10^{-9} A cm^{-2}
α_{an}	0.7
α_{cat}	1.7
γ_M	47

3.2. Model validation

Wang, Husar [56] have explored experimentally the effects of different operating environmental parameters. Using the

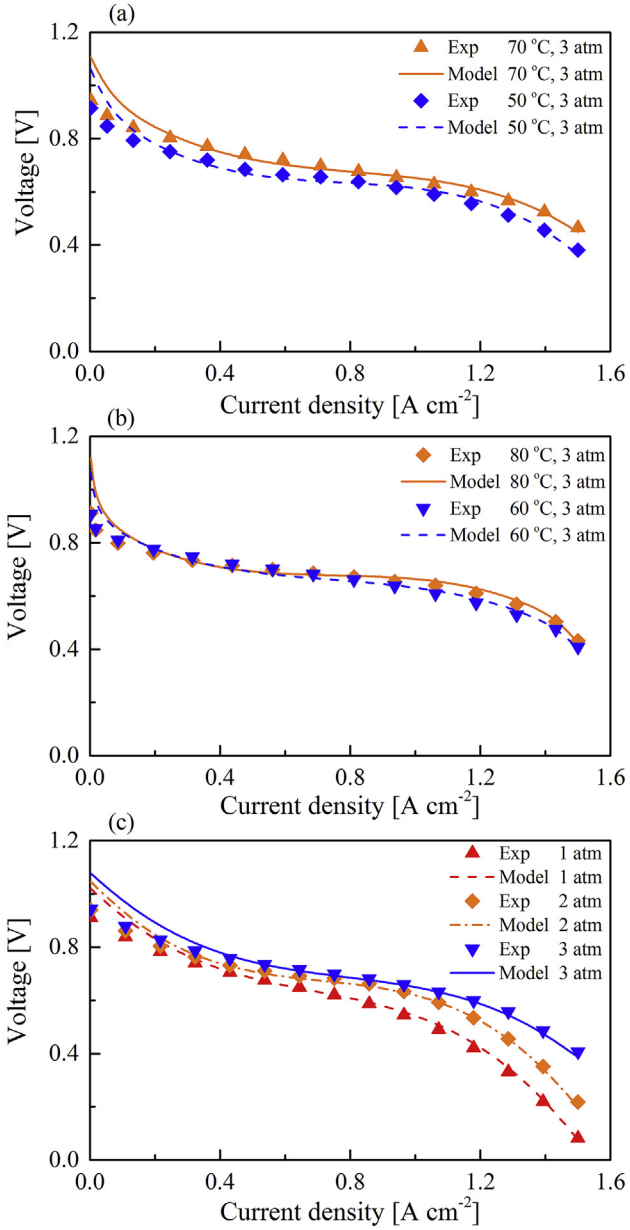

Fig. 5. Comparison between the model predictions and experimental results [56]. (a) constant pressure 3 atm with constant humidification temperature 70 °C, and cell temperatures 50 °C and 70 °C; (b) constant pressure 3 atm with humidification temperature equal to cell temperature at 60 °C and 80 °C; (c) varying pressure with constant humidification and cell temperature of 70 °C. All model parameters were held constant for changed environmental conditions.

parameter values listed in Tables 1 and 2, the predicted polarisation curve was compared to the experimental data from Ref. [56]. The model was fitted to the data for one combination of pressure, temperature and humidification and the predictions for different conditions were made with all parameters fixed. Fig. 5 shows the comparison between the fitted polarisation curves and the experimental data in at several temperatures and pressures. The generally good fit to the experimental data for all conditions confirms that the influences of environmental conditions are well modelled. The discrepancy in the region of activation polarisation (at low current density) is believed to be due to the reaction kinetics, as follows. In our simulation we adopted the values for activation energy and reference current density at standard test conditions from the literature. At low current density, however, the loading of electrocatalyst on the electrodes provides an alternative route for the reaction with a lower activation energy, which means the reaction kinetics becomes faster. As a result the activation overpotential decreases. Given that a real fuel cell is unlikely to be operated at such low power, this discrepancy can be regarded as minor.

The new model was also tested against three published models. Marr and Li [50] developed a PEM fuel cell model where they incorporated the electrochemical reactions in the catalyst layers, voltage losses and used engineering correlation for the process of reactant gas transport in the flow channels and through the electrodes. Corrêa, Farret [47] developed a dynamic electrochemical PEM fuel cell model based on voltage loss and power generation. Rowe and Li [68] developed a one dimensional non-isothermal model based on continuity, energy and the Stefan-Maxwell equation. Fig. 6 shows comparisons of the new model to the published models of the polarisation curve, made by adopting the model parameters from the particular published models [47,50,68]. Except at low current densities, the new model is at least as good as the published models.

3.3. Exploration of the polarisation curve

Fig. 7 shows the resulting polarisation curve and the various

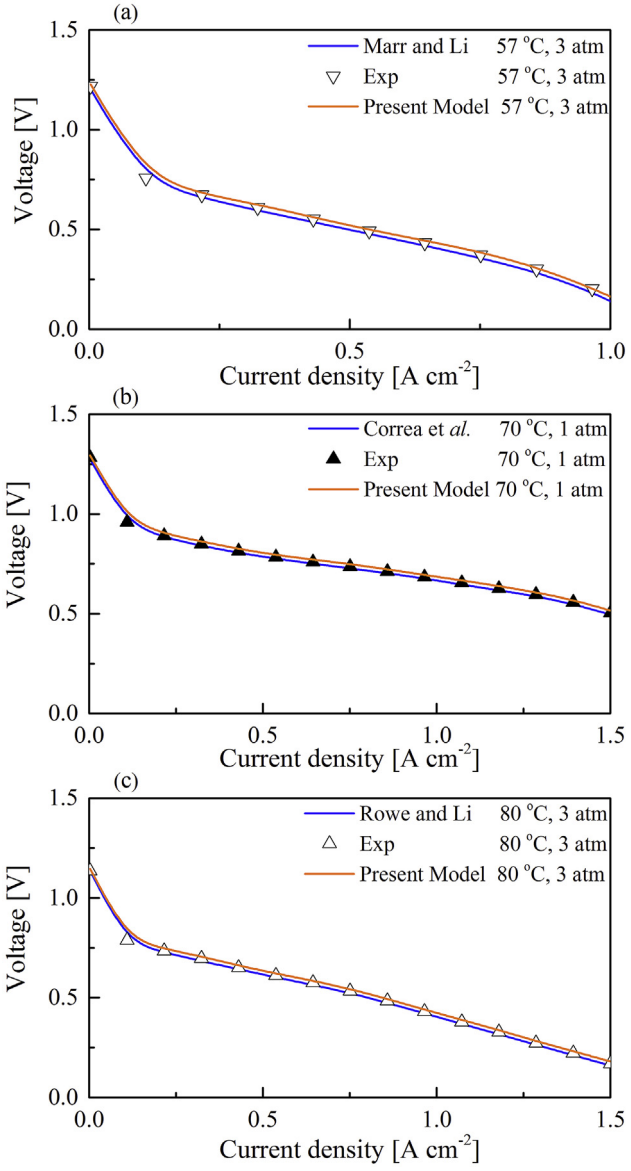

Fig. 6. Benchmarking this model against published models and experimental data. (a) Marr and Li [50]; (b) Corrêa, Farret [47]; (c) Rowe and Li [68].

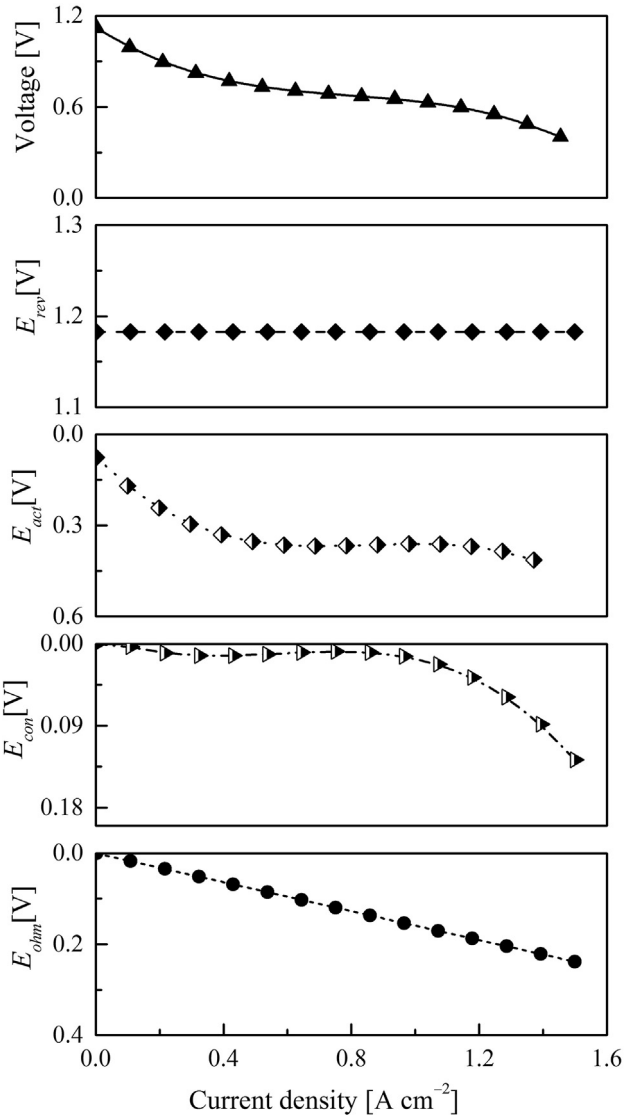

Fig. 7. Overpotential contributions to the polarisation curve for humidification temperature equal to cell temperature of 70 °C and pressure 1 atm.

overpotential contributions. The activation overpotential makes the highest contribution and reflects the sluggish electrode kinetics, principally due to the slow kinetics of the oxygen reduction reaction [69]. Second highest is the ohmic overpotential, which is mainly caused by ionic resistance, as discussed in § 2.4.4. The concentration/diffusion overpotential arises in mass diffusion limitations, and is therefore significant at high current densities and low reactant concentrations.

Fig. 8 shows the separate and combined effects of pressure and temperature on the polarisation curve of PEM fuel cell. Experimentally it is found that temperature has a greater influence on the cell performance than pressure [70] and Fig. 8 confirms this. It is apparent from Fig. 8 that under more extreme conditions of elevated pressure and elevated temperature, significantly higher power density is achievable within the fuel cell itself, although external factors such as the power needed to compress the reactant gases and shortened membrane lifetime may outweigh the benefit at the system level.

Management of water in the membrane is a crucial factor and a balance must be struck between sufficient membrane hydration and cathode flooding, in order to maintain a high rate of ionic transport and low mass transport resistance [28]. If the membrane is not properly hydrated (say λ>10), then at high current density the anode–membrane interface will become dehydrated, causing higher ionic resistance and, in extreme cases, irreversible damage. The degree of membrane hydration is affected by water transport across it (see § 2.3), which is related to the humidification of the inlet gases and the operating conditions [71]. Fig. 9 illustrates the very strong influence of PEM humidification on the polarisation curve. For λ=5 the loss of cell voltage at high current density is very significant.

Fig. 10 shows the polarisation curves for different relative humidification levels of inlet gases at the anode (hydrogen) and cathode (oxygen). Generally speaking, increasing humidification enhances the fuel cell performance. A high level of anode humidification is always beneficial (part (a) compared to part (b)) and for 100% anode humidification, decreased cathode humidification (part (b)) is fairly well tolerated, even for very low values (part (c)). On the other hand, excess cathode humidification leads to flooding in the cathode and loss of performance. Hence, high anode and moderate cathode humidification is the most robust combination.

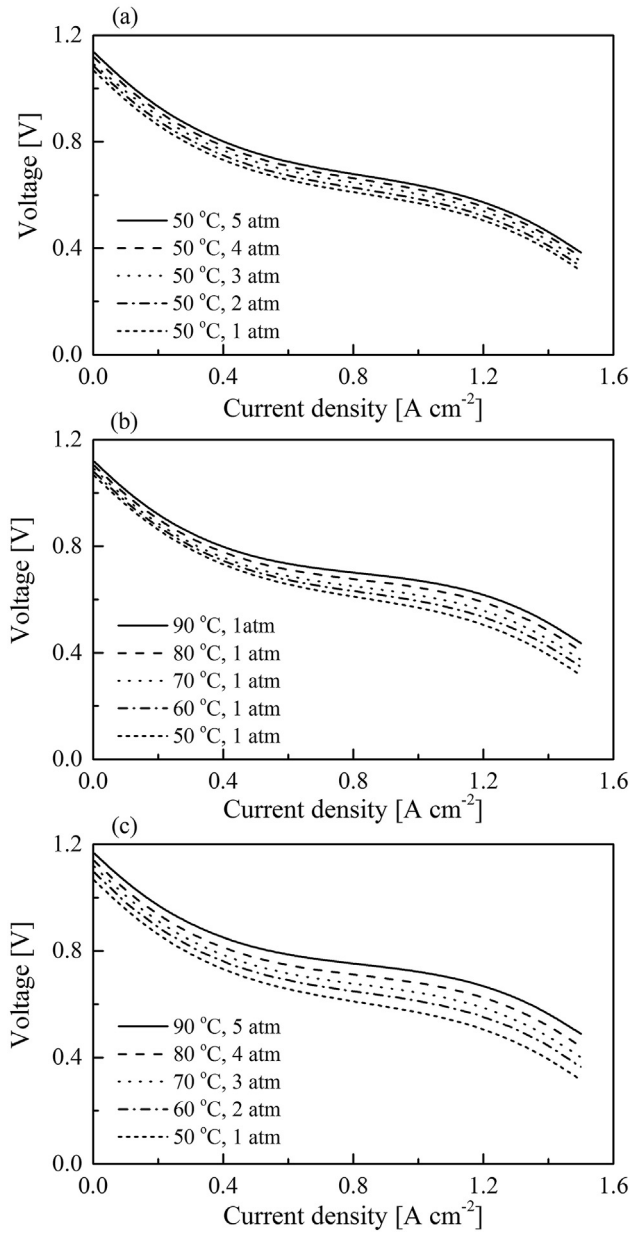

Fig. 8. Effects of temperature and pressure on polarisation curves for constant humidification temperature of 60 °C. (a) constant temperature and variable pressure; (b) constant pressure and variable temperature; (c) variable temperature and pressure, showing the significantly improved performance predicted for more extreme operating conditions.

4. Summary and conclusions

A steady-state one dimensional model of a PEM fuel cell based largely on physical parameters has been presented. This model is structured so that it can be easily extended to a stack of fuel cells and is modest in computing demand so that it can be incorporated in a whole-of-system simulation. Because the model relates PEM fuel cell performance to fundamental physical parameters, it can be utilised in developing improved electrodes to reduce the activation overpotential, for instance, by incorporating the measured or predicted characteristics of new electrocatalyst materials into the relevant ancillaries.

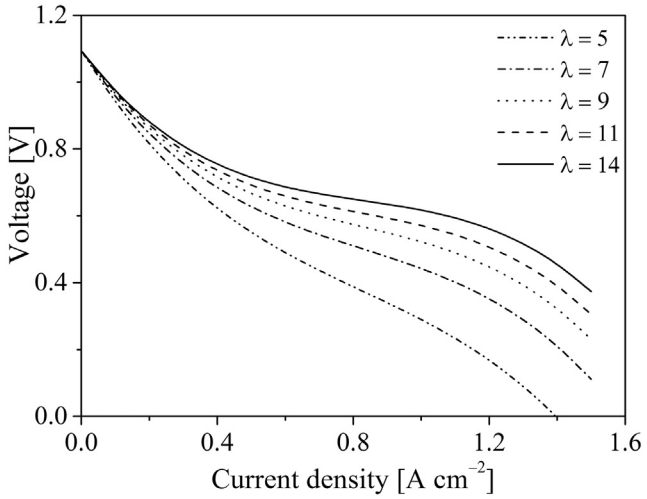

Fig. 9. Effect of PEM humidification for cell temperature of 70 °C, humidification temperature of 60 °C and pressure of 1 atm. Note the severe effect of humidification ratios (λ) below about 10.

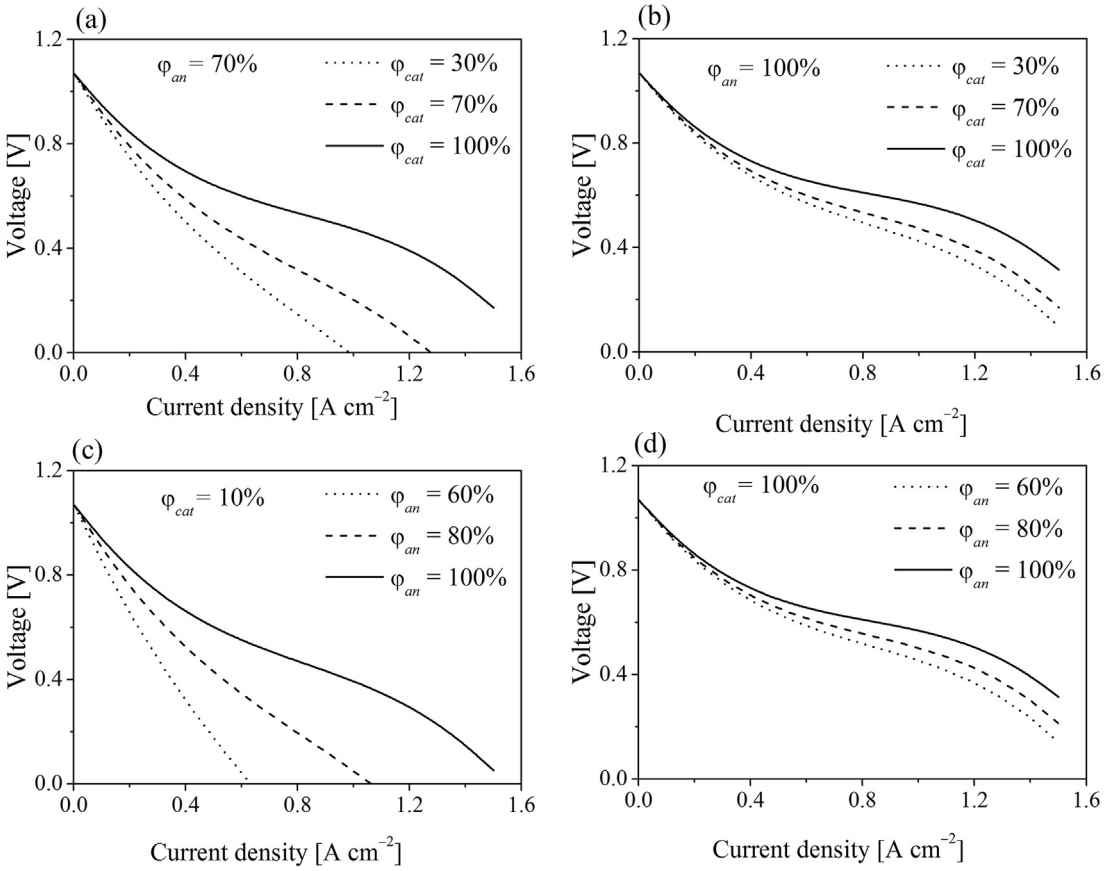

Fig. 10. Effects of anode and cathode humidities for cell temperature 50 °C, humidification temperature 60 °C and pressure 1 atm. (a) moderately anode humidification; (b) full anode humidification; (c) low cathode humidification; (d) full cathode humidification. Note the severe effect of combined low anode and low cathode humidification.

The mathematical model was validated in two ways. First, published experimental cell polarisation data were fitted very well, with five free model parameters (charge transfer coefficients, roughness factor and reference exchange current densities) related to physical parameters whose values are difficult to estimate reliably. The fitted values of these parameters were within the expected ranges. Importantly, the model also tracked changes in the polarisation curve owing to changed temperature and pressure, without altering the model parameters. Second, the model was also benchmarked against three published models with varying degrees of complexity and performed at least as well as these. Thus the approach using a simplified 1D model has been demonstrated to have good functionality.

A parametric study in which environmental input parameters (temperature, pressure, and reactant gas humidity) were varied demonstrated the ability of the model to reproduce the essential characteristics of a PEM fuel cell. In particular, the model showed how when the relative humidities of the feed gases were both reduced, the membrane became dehydrated and highly resistive.

A major remaining challenge is to develop a physically-based model to calculate the water uptake of the membrane in terms of the relative humidities of the feed gases and the cell temperature.

Acknowledgement

ZA acknowledges receipt of the Griffith University Postgraduate Research Scholarship and Griffith University International Postgraduate Research Scholarship.

References

[1] Yerramalla S, Davari A, Feliachi A, Biswas T. Modeling and simulation of the dynamic behavior of a polymer electrolyte membrane fuel cell. J Power Sources 2003;124(1):104–13.
[2] Ji M, Wei Z. A review of water management in polymer electrolyte membrane fuel cells. Energies 2009;2(4):1057–106.
[3] Bıyıkoğlu A. Review of proton exchange membrane fuel cell models. Int J Hydrogen Energy 2005;30(11):1181–212.
[4] Cheddie D, Munroe N. Review and comparison of approaches to proton exchange membrane fuel cell modeling. J Power Sources 2005;147(1):72–84.
[5] Djilali N, Lu D. Influence of heat transfer on gas and water transport in fuel cells. Int J Therm Sci 2002;41(1):29–40.
[6] Costamagna P. Transport phenomena in polymeric membrane fuel cells. Chem Eng Sci 2001;56(2):323–32.
[7] Dutta S, Shimpalee S, Van Zee J. Numerical prediction of mass-exchange between cathode and anode channels in a PEM fuel cell. Int J Heat Mass Transf 2001;44(11):2029–42.
[8] Wang Y, Wang C-Y. Simulation of flow and transport phenomena in a polymer electrolyte fuel cell under low-humidity operation. J Power Sources 2005;147(1):148–61.
[9] Ying W, Yang T-H, Lee W-Y, Ke J, Kim C-S. Three-dimensional analysis for effect of channel configuration on the performance of a small air-breathing proton exchange membrane fuel cell (PEMFC). J Power Sources 2005;145(2):572–81.
[10] Ying W, Sohn Y-J, Lee W-Y, Ke J, Kim C-S. Three-dimensional modeling and experimental investigation for an air-breathing polymer electrolyte membrane fuel cell (PEMFC). J power sources 2005;145(2):563–71.
[11] Lum KW, McGuirk JJ. Three-dimensional model of a complete polymer electrolyte membrane fuel cell–model formulation, validation and parametric studies. J Power Sources 2005;143(1):103–24.
[12] Hu M, Gu A, Wang M, Zhu X, Yu L. Three dimensional, two phase flow mathematical model for PEM fuel cell: Part I. Model development. Energy Convers Manag 2004;45(11):1861–82.
[13] Hu M, Zhu X, Wang M, Gu A, Yu L. Three dimensional, two phase flow mathematical model for PEM fuel cell: Part II. Analysis and discussion of the internal transport mechanisms. Energy Convers Manag 2004;45(11):1883–916.

[14] Carton JG, Olabi AG. Three-dimensional proton exchange membrane fuel cell model: comparison of double channel and open pore cellular foam flow plates. Energy 2016. http://dx.doi.org/10.1016/j.energy.2016.02.010. In Press.
[15] Ferreira RB, Falcão DS, Oliveira VB, Pinto AMFR. Numerical simulations of two-phase flow in an anode gas channel of a proton exchange membrane fuel cell. Energy 2015;82:619–28. http://dx.doi.org/10.1016/j.energy.2015.01.071.
[16] Carton JG, Lawlor V, Olabi AG, Hochenauer C, Zauner G. Water droplet accumulation and motion in PEM (Proton Exchange Membrane) fuel cell mini-channels. Energy 2012;39(1):63–73. http://dx.doi.org/10.1016/j.energy.2011.10.023.
[17] Kang S. Quasi-three dimensional dynamic modeling of a proton exchange membrane fuel cell with consideration of two-phase water transport through a gas diffusion layer. Energy 2015;90:1388–400. http://dx.doi.org/10.1016/j.energy.2015.06.076. Part 2.
[18] Xing L, Cai Q, Xu C, Liu C, Scott K, Yan Y. Numerical study of the effect of relative humidity and stoichiometric flow ratio on PEM (proton exchange membrane) fuel cell performance with various channel lengths: an anode partial flooding modelling. Energy 2016;106:631–45. http://dx.doi.org/10.1016/j.energy.2016.03.105.
[19] Salva JA, Iranzo A, Rosa F, Tapia E. Validation of cell voltage and water content in a PEM (polymer electrolyte membrane) fuel cell model using neutron imaging for different operating conditions. Energy 2016;101:100–12. http://dx.doi.org/10.1016/j.energy.2016.02.006.
[20] Abdollahzadeh M, Pascoa JC, Ranjbar AA, Esmaili Q. Analysis of PEM (Polymer Electrolyte Membrane) fuel cell cathode two-dimensional modeling. Energy 2014;68:478–94. http://dx.doi.org/10.1016/j.energy.2014.01.075.
[21] Liu H, Li P, Wang K. Optimization of PEM fuel cell flow channel dimensions—Mathematic modeling analysis and experimental verification. Int J Hydrogen Energy 2013;38(23):9835–46.
[22] Shekhar K. An investigation into the minimum dimensionality required for accurate simulation of proton exchange membrane fuel cells by the comparison between 1-and 3-dimension models. University of Cape Town; 2013.
[23] Abdin Z, Webb C, Gray EM. Solar hydrogen hybrid energy systems for off-grid electricity supply: a critical review. Renew Sustain Energy Rev 2015;52:1791–808.
[24] Abdin Z, Webb C, Gray EM. Modelling and simulation of a proton exchange membrane (PEM) electrolyser cell. Int J Hydrogen Energy 2015;40(39):13243–57.
[25] Mennola T, Noponen M, Aronniemi M, Hottinen T, Mikkola M, Himanen O, et al. Mass transport in the cathode of a free-breathing polymer electrolyte membrane fuel cell. J Appl Electrochem 2003;33(11):979–87.
[26] Mench MM. Fuel cell engines. John Wiley & Sons; 2008.
[27] Choi P, Jalani NH, Datta R. Thermodynamics and proton transport in nafion i. membrane swelling, sorption, and ion-exchange equilibrium. J Electrochem Soc 2005;152(3). E84–E9.
[28] Kumbur EC, Mench MM. Fuel cells – proton-exchange membrane fuel cells | water management A2-Garche, Jürgen. Encyclopedia of Electrochemical Power Sources. Amsterdam: Elsevier; 2009. p. 828–47.
[29] Springer TE, Zawodzinski T, Gottesfeld S. Polymer electrolyte fuel cell model. J Electrochem Soc 1991;138(8):2334–42.
[30] Onishi LM, Prausnitz JM, Newman J. Water-nafion equilibria. Absence of Schroeder's paradox. J Phys Chem B 2007;111(34):10166–73.
[31] Vallieres C, Winkelmann D, Roizard D, Favre E, Scharfer P, Kind M. On Schroeder's paradox. J Membr Sci 2006;278(1):357–64.
[32] Freger V. Hydration of ionomers and Schroeder's paradox in Nafion. J Phys Chem B 2008;113(1):24–36.
[33] Zawodzinski TA, Derouin C, Radzinski S, Sherman RJ, Smith VT, Springer TE, et al. Water uptake by and transport through Nafion® 117 membranes. J Electrochem Soc 1993;140(4):1041–7.
[34] LaConti A, Fragala A, Boyack J. Solid polymer electrolyte electrochemical cells-Electrode and other materials considerations. In: Conference Solid polymer electrolyte electrochemical cells-Electrode and other materials considerations, vol. 1; 1977. p. 354–74.
[35] Zawodzinski Jr TA, Neeman M, Sillerud LO, Gottesfeld S. Determination of water diffusion coefficients in perfluorosulfonate ionomeric membranes. J Phys Chem 1991;95(15):6040–4.
[36] Ni M, Leung MKH, Leung DYC. A modeling study on concentration over-potentials of a reversible solid oxide fuel cell. J Power Sources 2006;163(1):460–6. http://dx.doi.org/10.1016/j.jpowsour.2006.09.024.
[37] Hernández-Pacheco E, Singh D, Hutton PN, Patel N, Mann MD. A macro-level model for determining the performance characteristics of solid oxide fuel cells. J Power Sources 2004;138(1):174–86.
[38] Zhu H, Kee RJ. A general mathematical model for analyzing the performance of fuel-cell membrane-electrode assemblies. J Power Sources 2003;117(1):61–74.
[39] Reid RC, Prausnitz JM, Poling BE. The properties of gases and liquids. 1987.
[40] Chu L-Y, Park S-H, Yamaguchi T, Nakao S-i. Preparation of thermo-responsive core-shell microcapsules with a porous membrane and poly(N-isopropylacrylamide) gates. J Membr Sci 2001;192(1–2):27–39. http://dx.doi.org/10.1016/S0376-7388(01)00464-1.
[41] Ni M, Leung MK, Leung DY. An electrochemical model of a solid oxide steam electrolyzer for hydrogen production. Chem Eng Technol 2006;29(5):636–42.
[42] Larminie J, Dicks A, McDonald MS. Fuel cell systems explained. New York: Wiley; 2003.
[43] Amphlett JC, Baumert R, Mann RF, Peppley BA, Roberge PR, Harris TJ. Performance modeling of the Ballard Mark IV solid polymer electrolyte fuel cell I. Mechanistic model development. J Electrochem Soc 1995;142(1):1–8.
[44] Atkins PW, Atkins PW. The elements of physical chemistry. Oxford United Kingdom: Oxford University Press; 1992.
[45] Barbir F. Fuel cell basic chemistry, electrochemistry and thermodynamics. Mini-Micro Fuel Cells. Springer; 2008. p. 13–26.
[46] Biaku CY, Dale NV, Mann MD, Salehfar H, Peters AJ, Han T. A semiempirical study of the temperature dependence of the anode charge transfer coefficient of a 6 kW PEM electrolyzer. Int J Hydrogen Energy 2008;33(16):4247–54. http://dx.doi.org/10.1016/j.ijhydene.2008.06.006.
[47] Corrêa JM, Farret F, Canha LN, Simões MG. An electrochemical-based fuel-cell model suitable for electrical engineering automation approach. Ind Electron IEEE Trans 2004;51(5):1103–12.
[48] Marangio F, Santarelli M, Cali M. Theoretical model and experimental analysis of a high pressure PEM water electrolyser for hydrogen production. Int J Hydrogen Energy 2009;34(3):1143–58.
[49] Hwang J, Lai L, Wu W, Chang W. Dynamic modeling of a photovoltaic hydrogen fuel cell hybrid system. Int J Hydrogen Energy 2009;34(23):9531–42.
[50] Marr C, Li X. An engineering model of proton exchange membrane fuel cell performance. ARI Int J Phys Eng Sci 1998;50(4):190–200.
[51] Bernardi DM, Verbrugge MW. Mathematical model of a gas diffusion electrode bonded to a polymer electrolyte. AIChE J 1991;37(8):1151–63.
[52] Springer T, Wilson M, Gottesfeld S. Modeling and experimental diagnostics in polymer electrolyte fuel cells. J Electrochem Soc 1993;140(12):3513–26.
[53] Laurencelle F, Chahine R, Hamelin J, Agbossou K, Fournier M, Bose T, et al. Characterization of a Ballard MK5-E proton exchange membrane fuel cell stack. Fuel Cells 2001;1(1):66–71.
[54] Amphlett J, Baumert R, Mann R, Peppley B, Roberge P, Rodrigues A. Parametric modelling of the performance of a 5-kW proton-exchange membrane fuel cell stack. J Power Sources 1994;49(1):349–56.
[55] Nguyen TV, White RE. A water and heat management model for Proton-Exchange-Membrane fuel cells. J Electrochem Soc 1993;140(8):2178–86.
[56] Wang L, Husar A, Zhou T, Liu H. A parametric study of PEM fuel cell performances. Int J Hydrogen Energy 2003;28(11):1263–72.
[57] Thampan T, Malhotra S, Zhang J, Datta R. PEM fuel cell as a membrane reactor. Catal Today 2001;67(1):15–32.
[58] Aldebert P, Novel-Cattin F, Pineri M, Millet P, Doumain C, Durand R. Preparation and characterization of SPE composites forelectrolyzers and fuel cells. Solid State Ionics 1989;35(1):3–9.
[59] Damjanovic A, Brusic V. Electrode kinetics of oxygen reduction on oxide-free platinum electrodes. Electrochim Acta 1967;12(6):615–28.
[60] Beattie PD, Basura VI, Holdcroft S. Temperature and pressure dependence of O2 reduction at Pt| Nafion® 117 and Pt| BAM® 407 interfaces. J Electroanal Chem 1999;468(2):180–92.
[61] Parthasarathy A, Srinivasan S, Appleby AJ, Martin CR. Electrode kinetics of oxygen reduction at carbon-supported and unsupported platinum microcrystallite/Nafion® interfaces. J Electroanal Chem 1992;339(1):101–21.
[62] Nguyen PT, Berning T, Djilali N. Computational model of a PEM fuel cell with serpentine gas flow channels. J Power Sources 2004;130(1–2):149–57. http://dx.doi.org/10.1016/j.jpowsour.2003.12.027.
[63] Ju H, Meng H, Wang C-Y. A single-phase, non-isothermal model for PEM fuel cells. Int J Heat Mass Transf 2005;48(7):1303–15.
[64] Cheddie DF, Munroe ND. Three dimensional modeling of high temperature PEM fuel cells. J Power Sources 2006;160(1):215–23.
[65] Santarelli MG, Torchio MF, Cochis P. Parameters estimation of a PEM fuel cell polarization curve and analysis of their behavior with temperature. J Power Sources 2006;159(2):824–35.
[66] Walsh FC. A first course in electrochemical engineering. Electrochemical Consultancy; 1993.
[67] Barbir F. PEM fuel cells: theory and practice. Academic Press; 2012.
[68] Rowe A, Li X. Mathematical modeling of proton exchange membrane fuel cells. J Power Sources 2001;102(1):82–96.
[69] Nørskov JK, Rossmeisl J, Logadottir A, Lindqvist L, Kitchin JR, Bligaard T, et al. Origin of the overpotential for oxygen reduction at a fuel-cell cathode. J Phys Chem B 2004;108(46):17886–92.
[70] Murthy M, Esayian M, Lee W-k, Van Zee J. The effect of temperature and pressure on the performance of a PEMFC exposed to transient CO concentrations. J Electrochem Soc 2003;150(1):A29–34.
[71] Yan Q, Toghiani H, Wu J. Investigation of water transport through membrane in a PEM fuel cell by water balance experiments. J Power Sources 2006;158(1):316–25.